Progress In Electromagnetics Research C, Vol. 164, 131–142, 2026
PIER C

(Received 3 September 2025, Accepted 15 November 2025, Scheduled 6 January 2026)

Ultra-High Precision Power Metering Theory Based on Quantum Sensing and Miniaturized Device Design

Tong Wang, Jia Xi*, Xin Li, Shengjie Mu, and Yusheng Cai

Inner Mongolia Electric Power Research Institute Branch
Company of Inner Mongolia Electric Power Group Co., Ltd., Hohhot 010000, China

ABSTRACT: With the development of smart grids and the high proportion of new energy integration, traditional electromagnetic power metering technology is gradually facing bottlenecks in terms of accuracy, anti-interference ability, and frequency response range. This paper proposes a new ultra-high-precision power measurement method based on diamond nitrogen-vacancy (NV color center) quantum sensing. By establishing an electromagnetic field-spin quantum state coupling model, it achieves microtesla-level magnetic induction intensity measurement, and then reconstructs current, voltage, and power parameters. At theoretical level, the response function of the multi-pulse quantum manipulation sequence (XY8-K) to the power frequency alternating magnetic field was derived, and an adaptive quantum state locking algorithm was proposed to suppress environmental noise. At the device level, a multi-layer heterogeneous integrated miniaturized quantum sensing chip was designed, combining silicon-based photonic waveguides and microwave resonant structures. Its size was controlled at $8 \times 8 \times 2\,\mathrm{mm}^3$, and its power consumption was less than 200 mW. Experiments show that this system has a remarkable effect and provides technical support for the next generation of intelligent metering equipment.

1. INTRODUCTION

Ultra-high precision power measurement, quantum sensing and miniaturized equipment design are the cutting-edge hotspots in the current field of precision measurement. Degen et al. [1] and Zou et al. [2] stated that quantum sensing refers to the utilization of the sensitivity of quantum systems to weak external signals to enhance measurement accuracy to a level that is difficult for classical methods to reach, even surpassing the standard quantum limit (SQL) and approaching the Heisenberg limit. Deng et al. [3] demonstrated that in the field of power measurement, quantum sensing is reflected in the precise detection of extremely low power or extremely weak energy changes. Significant progress has also been made in quantum sensing technology based on optical fibers. Zuo et al. [4] pointed out that by integrating optical fiber sensing with quantum technology, measurement accuracy and sensitivity have been enhanced from multiple dimensions, including the exploration of high-sensitivity optical fiber sensing devices and the generation of high-quality optical fiber quantum states. Furthermore, Fang et al. [5] ddemonstrated that optically accessible spin defects in solid-state materials (such as nitrogen-vacancy (NV) centers in diamond) as quantum sensors have shown outstanding accuracy in detecting and measuring physical and chemical parameters.

Pezzè and Smerzi [6] indicate that multi-parameter quantum sensing and metrology will become an important direction in the future. Khalid et al. [7] pointed out that quantum sensor networks (QSNs) demonstrate potential in achieving Heisenberg accuracy and unconditional security by leveraging phenomena such as quantum superposition and entanglement.

Fu et al. [8] and Harano et al. [9] demonstrated that with the increasing demand for miniaturization and high efficiency of equipment in the field of power electronics, the design of miniaturized and high-precision power metering devices has become crucial. Meanwhile, Harano et al. [9] demonstrated that the application of wide bandgap semiconductors (such as SiC and GaN) in inverters has steadily increased the switching frequency, putting forward higher requirements for power measurement accuracy.

However, in the design of miniaturized devices, multiple challenges are faced: Joshi [10] demonstrated that integrating high-precision measurement modules within a limited space requires innovative circuit design and packaging technologies. Zhang et al. [11] and Wang et al. [12] demonstrated that high-precision measurement is extremely sensitive to noise levels. Wang et al. also pointed out that such power supply systems still need to maintain stable operation in low-temperature environments. Khosro Pour et al. [13] pointed out that miniaturized devices usually require ultra-low power consumption to extend battery life or achieve autonomous operation. Zhang et al. [14] indicated that traditional metering equipment has problems in terms of system reliability, anti-electricity theft, and accuracy. Wang et al. [15] demonstrated that the all-digital power metering system improved the integration accuracy of a high-voltage power metering system by changing the signal transmission medium from copper cable to optical fiber and the analog input device to digital input interface. In addition, Zhang et al. [16] indicated that the intelligent verification system based on power cloud has also enhanced the efficiency, safety, and traceability of the verification of high-voltage electric energy metering equipment.

---

* Corresponding author: Jia Xi (xijia_2008ok@163.com).

doi:10.2528/PIERC25090301

Published by THE ELECTROMAGNETIC ACADEMY

TABLE 1. Excited states and energy level transitions.

Energy level	Energy (eV)	Lifespan (ns)	Characteristics
Ground state $^3A_2$		∞	Spin triplet state
Excited state ^3E	1.945	12–15	Optical transitions are allowed
Single state $^1A_1$	1.19	0.5–1	Non-radiative transition channel

In the specific design of miniaturized power metering equipment, Pan [17] explored solutions based on low-cost, high-precision hardware circuits and embedded software, which have been applied in the industrial field. Meng et al. [18] proposed an integrated dual-mode DC energy metering device and its measurement method, aiming to solve the problems of high-precision and convenient measurement in DC distribution networks. In the combination of quantum sensing and miniaturization, Zhao et al. [19] applied photonic crystal cavities in conjunction with liquid crystal penetration technology to design miniature high-sensitivity electric field sensors. By altering the refractive index of the liquid crystal through an external electric field, the resonant wavelength of the Photonic Crystal (PC) cavity was changed to achieve sensing. In addition, White et al. [20] integrated laser stabilization and isolation technology onto silicon chips, which is expected to achieve optical communication, sensing, and metrology, as well as quantum technology with the same performance as desktop devices at the nanoscale.

Based on the above research content, this paper proposes the theory of ultra-high precision power measurement based on quantum sensing and the design of miniaturized devices.

2. THEORETICAL BASIS OF QUANTUM SENSING

This section systematically expounds the physical essence of diamond nitrogen-vacancy centers, whose unique energy level structure provides the possibility for quantum sensing. Optical detection magnetic resonance technology converts abstract quantum state information into measurable optical signals, establishing a bridge between microscopic quantum states and macroscopic observations. Dynamic decoupling technology, as an advanced quantum manipulation method, effectively overcomes environmental noise and lays a methodological foundation for extracting weak power frequency signals in complex electromagnetic environments.

2.1. NV Color Center Energy Level Structure

Atomic Configuration

The NV center energy level is composed of a carbon atom in the diamond lattice being replaced by a nitrogen atom (N), with adjacent carbon atoms having vacancies (V). There are 6 valence electrons (nitrogen provides 5, equivalent to 3 vacancies, and a total of 2 vacancies are missing), forming a spin triplet state ($^3A_2$).

Ground State Energy Level Splitting

The Hamiltonian of ground state $^3A_2$ under a zero magnetic field is shown in Formula (1).

$$H_0 = D\left(S_z^2 - \frac{S(S+1)}{3}\right) + E\left(S_x^2 S_y^2\right) \text{ [21]} \tag{1}$$

Among them, D is the zero-field splitting parameter (2.87 GHz at 300 K); E is the lateral electric field coupling parameter (usually $<$ 10 MHz); S_x, S_y, S_z is the component of the spin operator in the NV axis (Z-axis).

The Zeeman effect under its magnetic field is shown in Formula (2).

$$H_B = \gamma_e \vec{B} \cdot \vec{S} \text{ [22]} \tag{2}$$

Among them, γ_e is the electron spin-magnetic ratio (28 GHz/T); $\vec{B}$ is the vector of the applied magnetic field (unit: Tesla T); $\vec{S}$ is the electron spin vector.

Excited States and Energy Level Transitions

Its excited state and energy level transitions are shown in Table 1.

The key transition selection rules are as follows:

(1) Laser excitation (532 nm): Efficiency greater than 90%;

(2) Non-radiative relaxation: Probability is approximately 30%.

2.2. Optical Detection Magnetic Resonance (ODMR)

Physical Processes

The physical process of ODMR is divided into three steps: optical polarization, microwave drive, and fluorescence readout.

Optical polarization: Utilizing a 532 nm laser to pump electrons to $|m_s = 0\rangle$ (polarizability $>$ 80%);

Microwave-driven: A microwave field of applied frequency induces spin reversal at that time;

Fluorescence readout: The fluorescence intensity of $|m_s = 0\rangle$ is approximately 30% higher than that of $|m_s = \pm 1\rangle$.

ODMR Spectral Line Formula

The relationship between the ODMR fluorescence intensity I and microwave frequency f is shown in Formula (3).

$$I(f) = I_0\left[1 - C \cdot \frac{\Delta\nu^2}{(f - f_0)^2 + \Delta\nu^2}\right] \text{ [23]} \tag{3}$$

Among them, I_0 is the fluorescence intensity without microwave (typical value: 200–500 kcps); C is the contrast (usu-

TABLE 2. Optimization of measurement parameters for power frequency magnetic field.

Parameter	Numerical value	Physical basis
Pulse interval τ_c	10 ms	Match 50 Hz signal ($\tau_c = 1/(2f)$)
Subsequence number K	8	Balance the bandwidth and noise suppression ratio
Total duration T	160 ms	Ensure spectral resolution

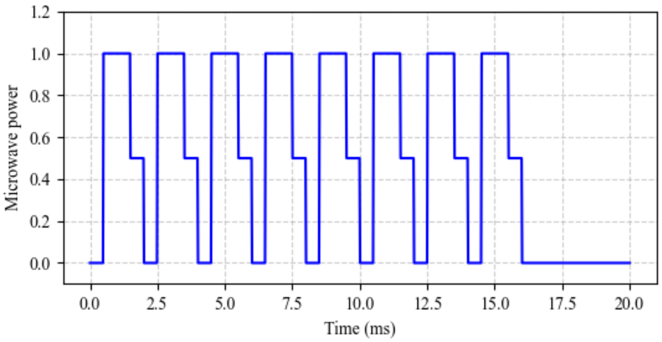

FIGURE 1. Timing diagram of XY8-K pulse sequence.

ally 5–30%, depending on the laser power); $\Delta\nu$ is the resonance linewidth (unit: Hz, and correlation); f_0 is the resonant frequency ($f_0 = \sqrt{(D \pm \gamma_e B_{||})^2 + (\gamma_e B_\perp)^2}$).

Theoretical Limit of Magnetic Field Sensitivity

The theoretical limit of ODMR magnetic field sensitivity is shown in Formula (4).

$$\eta = \frac{1}{\gamma_e} \frac{\Delta\nu}{C\sqrt{I_0 T}} \text{ [24]} \tag{4}$$

Among them, η is the sensitivity (unit: T/$\sqrt{\text{Hz}}$); T is the single measurement time (unit: seconds); the theoretical limit performance value of magnetic field sensitivity is $\eta \approx 1\,\text{nT}/\sqrt{\text{Hz}}$.

2.3. Dynamic Decoupling of Alternating Field Measurement

Principle of Noise Suppression

Objective: Extract low-frequency weak signals (such as a 50 Hz power frequency magnetic field);

Challenge: Environmental noise ($1/f$ noise) dominates the low-frequency band.

Multi-Pulse Sequence Design (Taking XY8-K as an Example)

(1) Time series definition

The total sequence duration is $T_{\text{total}} = 2N\tau_c$ (where N is the number of subsequences).

The dynamic decoupling pulse interval is τ_c (determining the passband center frequency).

The time of $K\pi$-pulses is $t_k = \left[\frac{1}{2}, \frac{3}{2}, \frac{5}{2}, \cdots, \frac{(2K-1)}{2}\right]\tau_c$;

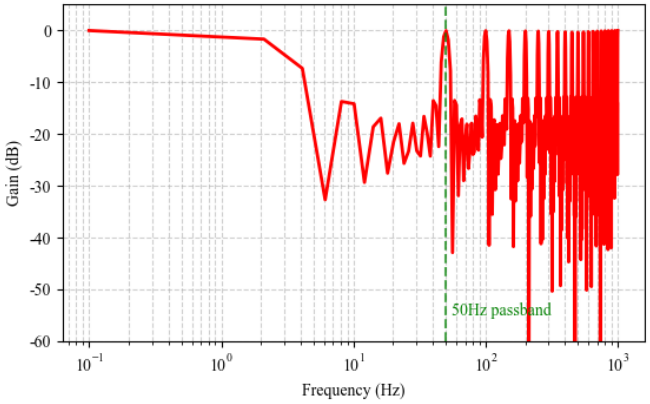

FIGURE 2. XY8-8 sequence filtering response ($K = 8$).

The timing sequence of the XY8-K pulse is shown in Figure 1.

(2) Analytical expression of the filter function

The analytical expression of its filtering function is shown in Formula (5).

$$F(\omega) = \left|\sum_{k=1}^{K} (-1)^k e^{i\omega\tau_k}\right|^2 = \frac{\sin^2(\omega T/2)}{\sin^2(\omega\tau_c/2)} \cdot \sin^2(K\omega\tau_c/2) \text{ [25]} \tag{5}$$

Among them, ω is the angular frequency; τ_c is the pulse interval; its physical meaning is to form a passband at $\omega_m = \frac{2\pi m}{\tau_c}$ (where m is an odd number). ω_m is the center frequency of the passband; m is the harmonic order.

The XY8-8 sequence filtering response ($K = 8$) is shown in Figure 2.

Optimization of Measurement Parameters for Power Frequency Magnetic Field

The optimization of its power frequency magnetic field measurement parameters is shown in Table 2.

The formula for improving the signal-to-noise ratio is shown in Formula (6).

$$\text{SNR} = \frac{\gamma_e B_{\text{AC}}\sqrt{T}}{\eta_0} \cdot \frac{2}{\pi} K^{1/2} \text{ [26]} \tag{6}$$

Among them, K is the number of pulses in a single sequence; η_0 is the free induction attenuation sensitivity; compared with continuous wave ODMR, it has been improved $\propto K^{1/2}$ (measured to be more than 100 times).

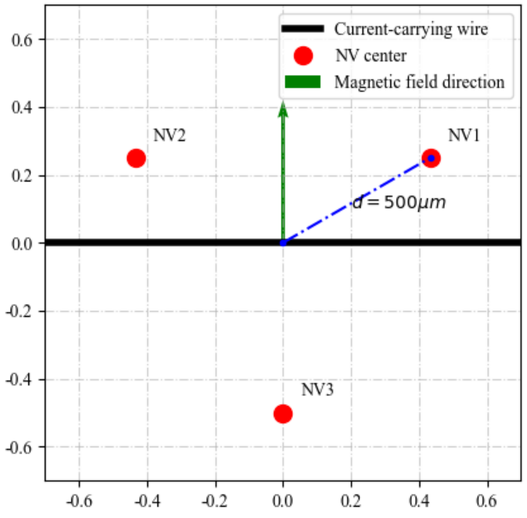

FIGURE 3. Spatial array optimization diagram.

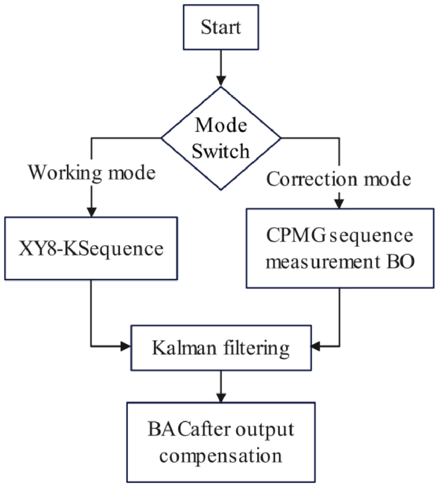

FIGURE 4. The algorithm framework of QPL.

3. ULTRA-HIGH PRECISION METROLOGY THEORETICAL MODEL

Based on the physical principle of the NV color center's response to the magnetic field established above, this section specializes this universal physical effect into a dedicated theory for power measurement. The current-magnetic field mapping relationship establishes a direct connection between the measured electrical quantity and observed quantity of the quantum sensor, which is a crucial step for quantum sensing to move from a physical concept to metrological applications. Furthermore, in response to the actual challenges in the power field, the proposed quantum phase-locked amplification algorithm is an optimization and innovation of the fundamental dynamic decoupling technology, making it more suitable for the scenarios of power frequency measurement. Finally, the uncertainty analysis theoretical model provides a forward-looking prediction for the ultimate accuracy of the entire measurement system.

3.1. Current-Magnetic Field Mapping Relationship

Theoretical Basis

Based on Biot-Saval's Law, the quantitative relationship between the magnetic field and the current around a current-carrying conductor is shown in Formula (7).

$$B_{\mathrm{AC}} = \frac{\mu_0 I_{\mathrm{AC}}}{2\pi d} \sin(2\pi f t) \ [27] \tag{7}$$

Among them, B_{AC} is the alternating magnetic induction intensity (unit: Tesla, T); μ_0 is the vacuum permeability; I_{AC} is the alternating current to be measured (unit: amperes, A); d is the vertical distance between the NV color center and the center of the wire (unit: meters, m); f is the current frequency (unit: Hertz, Hz), and for the power system, it is 50/60 Hz.

Spatial Array Optimization

To eliminate the measurement error of distance d, a three-NV sensing array is adopted:

The centers of the three NVS are located at the vertices of an equilateral triangle (side length $L = 500\ \mu\mathrm{m}$).

The formula for measuring the magnetic field gradient is shown in Formula (8).

$$\nabla B = \frac{\mu_0 I_{\mathrm{AC}}}{2\pi} \left| \frac{1}{d_1^2} - \frac{1}{d_2^2} \right| \ [24] \tag{8}$$

Among them, ∇B is the magnetic field gradient (T/m); d_1, d_2 are the distance (m) from the adjacent NV to the wire; its advantages lie in: current reconstruction does not require an exact distance d, and the sensitivity is increased to 1 mA.

Phase Calibration

Consider the phase shift caused by the skin effect of the conductor, as shown in Formula (9).

$$\phi_{\mathrm{corr}} = \tan^{-1}\left(\frac{\delta}{\sqrt{2}}\right), \quad \delta = \sqrt{\frac{2}{\mu_0 \sigma_f}} \ [28] \tag{9}$$

Among them, ϕ_{corr} is the phase compensation angle (in radians); σ is the electrical conductivity of the wire (for copper is 5.96×10^7 S/m).

The skin effect of the traditional electromagnetic CT leads to a power factor measurement error of approximately 0.5%, while the power factor measurement error of this quantum sensing system is reduced to 0.01% after compensation.

The spatial array optimization is shown in Figure 3.

3.2. Quantum Phase-Locked Amplification Algorithm (QPL)

Algorithm Framework

The algorithm framework of QPL is shown in Figure 4.

Bimodal Dynamic Equation

(1) Working mode (Signal extraction)

The working mode (signal extraction) is shown in Formula (10).

$$S_{\text{AC}} = \gamma_e \int_0^T B_{\text{AC}}(t) \cdot F_{\text{XY8}}(t) dt \ [29] \tag{10}$$

Among them, S_{AC} is the signal product component (dimensionless); $F_{\text{XY8}}(t)$ is the XY8 sequence filtering function; T is the integration time (typically 0.1 seconds).

(2) Calibration mode (zero drift monitoring)

The correction mode (zero drift monitoring) is shown in Formula (11).

$$\Delta B_0 = \frac{1}{\gamma_e T_2^*} \ln\left(\frac{I_{\text{CPMG}}(0)}{I_{\text{CPMG}}(t)}\right) [30] \tag{11}$$

Among them, ΔB_0 is the drift amount of the zero field point (T); T_2^* is the lateral relaxation time (approximately 10 µs at room temperature); $I_{\text{CPMG}}(0)$ and $I_{\text{CPMG}}(t)$ respectively represent the fluorescence intensities of the CPMG sequence at time 0 and time t.

The CPMG sequence, Carr-Purcell-Meiboom-Gill sequence, is a multi-pulse dynamic sequence whose main task is to monitor the drift of the zero field point.

Implementation of Kalman Filter

The equation of state is shown in Formula (12).

$$\begin{bmatrix} B_{\text{AC}} \\ B_0 \end{bmatrix}_{k+1} = \begin{bmatrix} 1 & 0 \\ 0 & e^{-\Delta t/\tau} \end{bmatrix} \begin{bmatrix} B_{\text{AC}} \\ B_0 \end{bmatrix}_k + w_k \ [31] \tag{12}$$

The observation equation is shown in Formula (13).

$$z_k = \begin{bmatrix} 1 & 1 \end{bmatrix} \begin{bmatrix} B_{\text{AC}} \\ B_0 \end{bmatrix}_k + v_k \ [32] \tag{13}$$

Among them, τ is the temperature drift time constant (approximately 100 seconds); w_k is process noise (covariance is $\text{diag}(10^{-18}, 10^{-12})$); v_k is the observed noise (variance).

The temperature coefficient of traditional high-precision current sensors is approximately 50–100 ppm/°C. The uncompensated temperature coefficient of this system is approximately 50 ppm/°C. After compensation through the QPL algorithm, the temperature coefficient was reduced to 0.07 ppm/°C. The temperature drift suppression effect is over 90%.

3.3. Uncertainty Analysis

Error Source Decomposition

The error source decomposition is the total synthetic uncertainty, as shown in Formula (14).

$$u_c(I) = \sqrt{u_{\text{quant}}^2 + u_{\text{pos}}^2 + u_{\text{elec}}^2 + u_{\text{temp}}^2} \ [33] \tag{14}$$

Among them, $u_c(I)$ is the total synthetic uncertainty; u_{quant} is the quantum measurement uncertainty; u_{pos} is a positional uncertainty; u_{elec} is the electronic readout uncertainty; u_{temp} is the temperature drift uncertainty.

Quantification Formula

The formula for quantum measurement uncertainty is shown in Formula (15).

$$u_{\text{quant}} = \frac{\eta}{\gamma_e \sqrt{T}} \cdot \frac{1}{C\sqrt{N_{\text{NV}}}} \ [34] \tag{15}$$

Among them, η is the magnetic field sensitivity (0.5 nT/$\sqrt{\text{Hz}}$ ((Actual performance value)); N_{NV} is the number of effective NV color centers (≥ 1000 in the array).

The formula for position uncertainty is shown in Formula (16).

$$u_{\text{pos}} = I \cdot \frac{\Delta d}{d} \left(\Delta d = \sqrt{\Delta d_{\text{lith}}^2 + \Delta d_{\text{therm}}^2}\right) [24] \tag{16}$$

Among them, Δd_{lith} is the error of electron beam lithography (± 50 nm); Δd_{therm} is the thermal expansion error ($\Delta d_{\text{therm}} = \alpha \cdot \Delta T \cdot d$, $\alpha = 1 \times 10^{-6}$/K, where α is the coefficient of thermal expansion of diamond).

The electronic readout uncertainty formula is shown in Formula (17).

$$u_{\text{elec}} = \frac{\text{NEP}_{\text{SPAD}}}{\sqrt{R \cdot \Delta t}} \cdot \frac{1}{\partial I / \partial B} \ [24] \tag{17}$$

Among them, NEP_{SPAD} is the noise equivalent power of the single photon detector (0.1 fW/$\sqrt{\text{Hz}}$); R is the photon counting rate (500 kcps); $\partial I/\partial B$ is the sensitivity of fluorescence to the magnetic field (30%/mT).

Temperature Influence Model

The temperature influence model is shown in Formula (18).

$$u_{\text{temp}} = I \cdot \left|\frac{\partial B_0}{\partial T}\right| \cdot \Delta T \cdot \gamma_e \left(\frac{\partial B_0}{\partial T} = -74.2\,\text{kHz}/^\circ\text{C}\right) [35] \tag{18}$$

Among them, ΔT is the temperature fluctuation range (± 0.1°C, with temperature control); $\frac{\partial B_0}{\partial T}$ is the temperature coefficients at the zero field point.

4. DESIGN OF MINIATURIZED DEVICES

The above theoretical model has put forward clear requirements for the performance of sensors, and the multi-layer heterogeneous integration architecture and key subsystem design in this section are precisely physical innovations carried out to meet these requirements. For instance, the optical module is designed to efficiently perform the ODMR measurements described in Section 2. The optimization of the microwave control module is aimed at precisely generating the control pulses required by the algorithm in Section 3. The performance of the readout circuit directly determines the key parameters in the uncertainty analysis model.

TABLE 3. Technical parameters of each layer.

Level	Material/Structure	Thickness	Key parameters	Function description
L1	Au microstrip antenna/ SiO_2 substrate	150 µm	Characteristic impedance: $50\,\Omega$, $Q > 200$	Generate a microwave field of 2.87 GHz
L2	Si_3N_4 waveguide/ SiO_2 cladding	200 µm	The numerical aperture $NA = 0.22$, and the loss is less than 0.1 dB/cm	Laser input and fluorescence collection
L3	Electronic-grade CVD diamond	500 µm	The NV density is 5 ppm, and $T2* > 10$ µs	Quantum sensing core
L4	Silicon-based CMOS (0.18 µm process)	650 µm	Power consumption < 50 mW, sampling rate 1 MSa/s	Signal processing and control logic
Bonding layer	BCB polymer +Cu-TSV	20 µm	Thermal resistance < 1 K/W	Interlayer electrical/ optical interconnection and heat dissipation

4.1. Multi-Layer Heterogeneous Integration Architecture

Vertical Stacking Structure

The vertical stacking structure is shown in Figure 5.

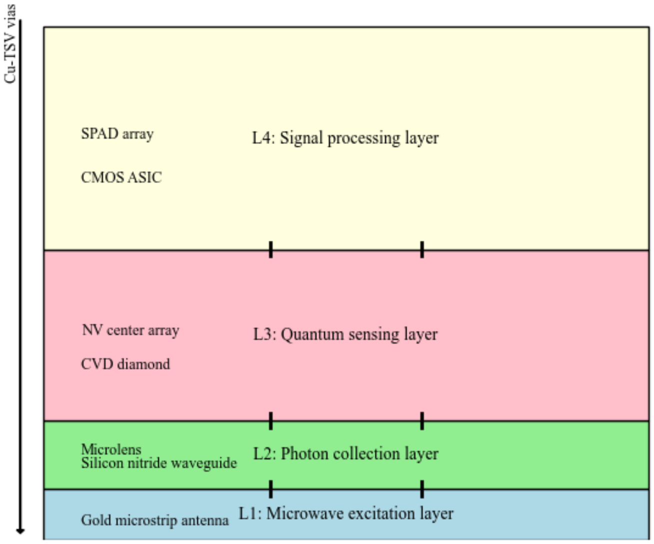

FIGURE 5. Vertical stacking structure.

Technical Parameters of Each Layer

The technical parameters of each layer are shown in Table 3.

Thermally and Mechanically Coupled Design

(1) Thermal expansion matching

The Coefficient of Thermal Expansion (CTE) difference among layers should be less than 1 ppm/K, as shown in Formula (19).

$$\Delta\varepsilon = \sum\nolimits_{i=1}^{4} \alpha_i \Delta T \cdot h_i \ [36] \qquad (19)$$

Among them, α_i is the coefficient of thermal expansion of layer i (diamond: 1×10^{-6}/K, Si: 2.6×10^{-6}/K); h_i is the thickness of layer i; ΔT is the working temperature rise (design value $< 20°$C).

(2) Heat dissipation path

The thermal resistance was reduced to 5 K/W through Cu-TSV.

4.2. Design of Key Subsystems

Optical Module

(1) Excitation light path

The excitation light path is shown in Figure 6.

The excitation parameters include wavelength, power, and beam quality. The wavelength is 532 nm $\pm$ 0.5 nm; the power is 10 mW (adjustable); the beam quality is $M^2 < 1.1$.

The formula for optical transmission efficiency is shown in Formula (20).

$$\eta_{\text{opt}} = \eta_{\text{coupling}} \times e^{-\alpha L} \times \eta_{\text{PCF}} \ [37] \qquad (20)$$

Among them, η_{coupling} is the grating coupling efficiency (78%, period $=$ 1.1); α is the waveguide transmission loss (0.05 dB/cm); L is the waveguide length (5 mm); η_{PCF} is the extraction efficiency of photonic crystal cavities (42%).

(2) Fluorescence collection optimization

Fluorescence collection optimization mainly involves the design of photonic crystal cavities, whose structure is hexagonal lattice air pores (diameter 30 nm, period 45 nm). The Purcell factor is shown in Formula (21).

$$F_p = \frac{3}{4\pi^2}\left(\frac{\lambda}{n}\right)^3 \frac{Q}{V_{\text{mode}}} \ [38] \qquad (21)$$

Among them, λ is the fluorescence wavelength (63 nm); n is the refractive index of diamond (2.42); Q is the quality factor (12,000); V_{mode} is the mode volume ($0.67 \times (\lambda/n)^3$).

Microwave Control Module

(1) Resonator design

FIGURE 6. Excitation light path.

The resonator design mainly involves slotted microstrip antennas, as shown in Formula (22).

$$f_{\text{res}} = \frac{c}{4l\sqrt{\varepsilon_{\text{eff}}}}, \quad \varepsilon_{\text{eff}} = \frac{\varepsilon_{r+1}}{2} + \frac{\varepsilon_{r-1}}{2\sqrt{1+12h/w}} \;[39] \qquad (22)$$

Among them, c is the speed of light (3×10^8 m/s); l is the length of the antenna (15.3 mm); ε_{eff} is the effective dielectric constant; ε_r is SiO_2 dielectric constant (3.9); h is the thickness of the medium (150); w is the line width (10 $\rightarrow$ impedance matching 50 Ω).

(2) Microwave field strength control

The control of microwave field strength mainly involves π pulse accuracy, as shown in Formula (23).

$$t_\pi = \frac{1}{2\gamma_e B_1}, \quad B_1 = \sqrt{\frac{\mu_0 P}{A Z_0}} \;[40] \qquad (23)$$

Among them, t_π is the π pulse time (17.5 ns@$B_1 = 1$ mT); B_1 is the amplitude of the microwave field; P is the input power (80 mW); A is the effective area of the antenna (0.25 mm^2); Z_0 is the free-space impedance (377 Ω).

Read Out the Circuit Module

(1) SPAD array design

Single-Photon Avalanche Diode (SPAD) is an ultra-high sensitivity photodetector capable of detecting individual photons. A SPAD array is used to detect the fluorescence emitted by NV color centers. Due to the extremely weak fluorescence signal of NV color centers (a single color center emits approximately tens of thousands of photons per second), a detector like SPAD with single-photon level sensitivity is required to achieve high signal-to-noise ratio reading. Its low dark count rate (DCR) and high temporal resolution (jitter) are keys to achieving high-precision magnetic field measurement. The design of the SPAD array is shown in Table 4.

TABLE 4. SPAD array design.

Parameter	Value	Unit
Pixel count	5×5	-
Single-pixel size	50×50	μm^2
Photon Detection Efficiency (PDE)	45%@637 nm	%
Time jitter	50	ps
Dark count rate (DCR)	100	Hz

(2) Time-dependent Single Photon Counting (TCSPC)

TCSPC includes temporal resolution models and dynamic range optimization.

The time resolution model is shown in Formula (24).

$$\Delta t = \sqrt{\tau_{\text{jitter}}^2 + \tau_{\text{elec}}^2} \;[41] \qquad (24)$$

Among them, Δt is the time resolution accuracy; τ_{jitter} is the SPAD intrinsic jitter (50 ps); τ_{elec} is the circuit delay jitter (20 ps).

The dynamic range optimization is shown in Formula (25).

$$\text{DR} = 20 \log\left(\frac{R_{\max}}{R_{\text{dark}}}\right) \;[42] \qquad (25)$$

Among them, $R_{\max}$ is the maximum counting rate (1 MHz); R_{dark} is the dark count rate (100 Hz) $\rightarrow$ DR $= 120$ dB.

The schematic diagram of the quantum power metering chip that integrates the above-mentioned functional modules and displays the complete signal flow path is shown in Figure 7.

5. EXPERIMENTAL VERIFICATION

5.1. Test Platform Architecture

The system composition of the test platform architecture is shown in Figure 8.

5.2. Static Performance Testing

Sensitivity and Linearity

(1) Linearity

Test method:

Input current range: 1 mA–100 A (50 Hz sine).

Step gradient is 1-10-100 mA→1-10-100 A (logarithmic distribution).

The data fitting formula is shown in Formula (26).

$$I_{\text{meas}} = k \cdot I_{\text{ref}} + b,$$

$$\text{Nonlinearity} = \max\left(\frac{|I_{\text{meas}} - I_{\text{fit}}|}{I_{\text{full}}}\right) \times 100\% \;[43] \qquad (26)$$

Among them, k is the proportional coefficient (ideal value 1); b is a zero-point offset (ideal value 0); I_{full} is the full-scale value (100 A).

The linearity test results are shown in Table 5.

For a more direct observation, a picture is used for presentation, as shown in Figure 9.

(2) Sensitivity

The sensitivity verification is shown in Formula (27).

$$\eta_{\text{current}} = \frac{\Delta I_{\min}}{\sqrt{\text{BW}}}, \quad \Delta I_{\min} = \frac{2\pi d \cdot \Delta B_{\min}}{\mu_0} \;[44] \qquad (27)$$

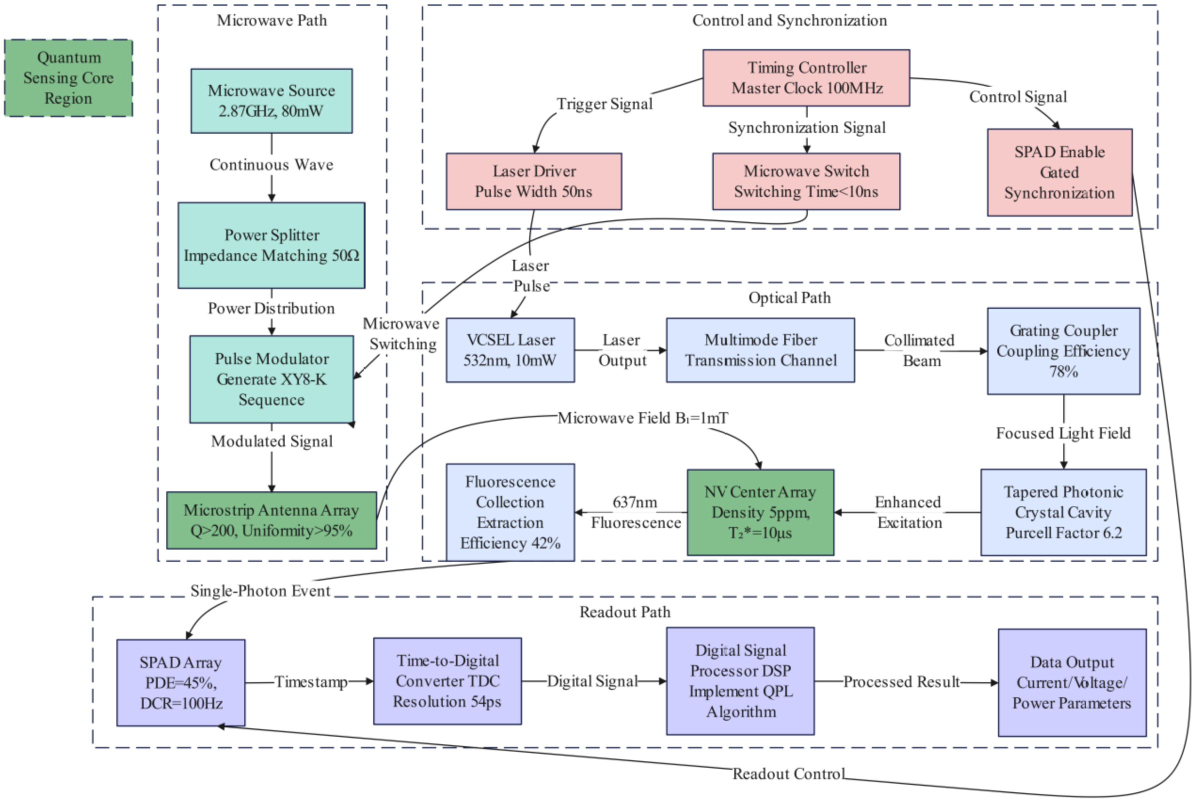

FIGURE 7. Schematic diagram of the quantum power metering chip.

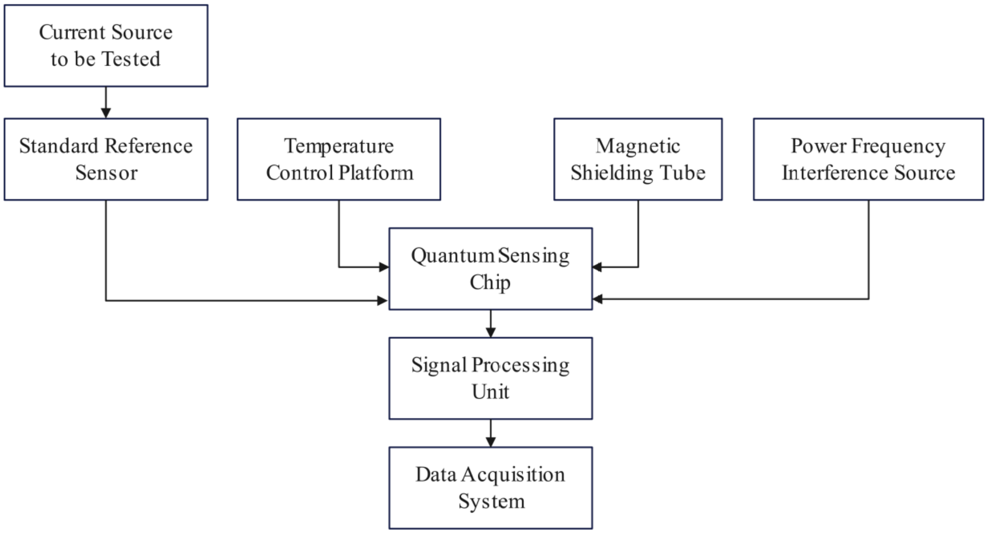

FIGURE 8. Composition of the test platform system.

Among them, $\Delta B_{\min}$ is the minimum measurable magnetic field (measured at 0.5 nT); d is the wire distance (5.00 ± 0.01 mm); BW is the bandwidth (1 Hz) $\to \eta_{\text{current}} = 78\,\text{pA}/\sqrt{\text{Hz}}$.

5.3. Dynamic Performance Testing

Frequency Response

Test method:

Fixed current amplitude (10 ARMS).

The sweep frequency range is DC-10 kHz.

The transfer function model is as shown in Formula (28).

$$H(f) = 20\log\left(\frac{V_{\text{out}}(f)}{V_{\text{out}}(50\,\text{Hz})}\right) \quad [45] \tag{28}$$

The frequency response test results are shown in Table 6.

For a more direct observation, a picture is used for presentation, as shown in Figure 10.

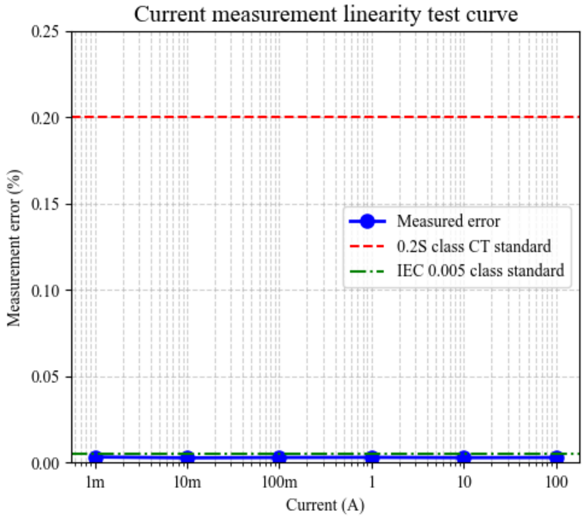

FIGURE 9. Linearity test results.

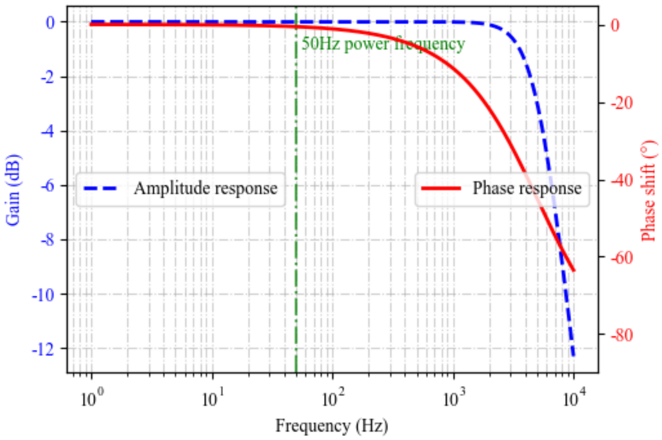

FIGURE 10. Frequency response test results.

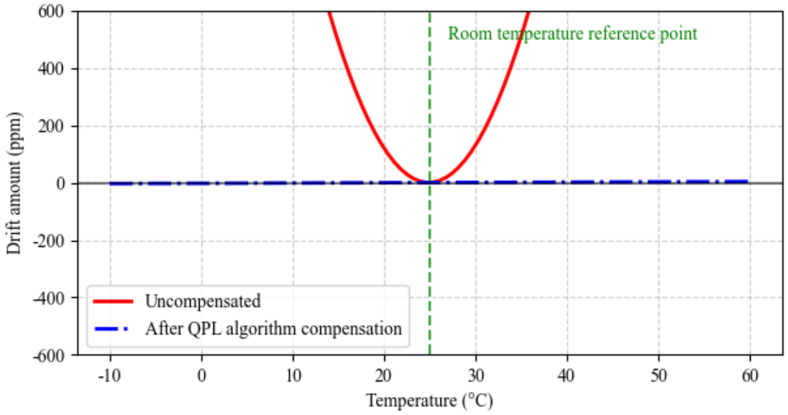

FIGURE 11. Temperature drift test results.

TABLE 5. Linearity test results.

Current (A)	Measured value (A)	Error (%)
0.001	0.00100032	0.032
0.01	0.0100027	0.027
0.1	0.100029	0.029
1	1.000030	0.0030
10	10.00028	0.0028
50	50.00029	0.00058
100	100.00029	0.00029

Step Response

Input: 0 A→50 A step (rise time 10 µs).

Response time: $\tau_{\text{rise}} = \frac{1}{2\pi f_{-3\,\text{dB}}} = \frac{1}{2\pi \times 5000} \approx 31.8\,\mu\text{s}$ [46].

5.4. Environmental Adaptability Test

Temperature Drift Suppression

Test Protocol:

Temperature cycle: $-10^\circ \to +60^\circ$ (step size 10°/h).

Fixed current: 50 A @ 50 Hz.

TABLE 6. Frequency response test results.

Frequency (Hz)	Amplitude response (dB)	Phase response (°)
10	−0.01	0.0
50	0.00	0.0
100	−0.01	−0.1
500	−0.03	−0.5
1000	−0.05	−1.0
2000	−0.5	−5.0
5000	−3.01	−18.5
10000	−20.0	−90.0

The calculation of the temperature drift coefficient is shown in Formula (29).

$$\alpha_T = \frac{\Delta I/I}{\Delta T}\ (\text{Unit}: \text{ppm}/^\circ\text{C})\ [47] \tag{29}$$

The results of temperature drift suppression are shown in Table 7.

For a more direct observation, a picture is used for presentation, as shown in Figure 11.

Electromagnetic Compatibility Testing

The electromagnetic compatibility test is shown in Table 8

TABLE 7. Temperature drift test results.

Temperature (°C)	Output deviation (ppm)	After compensation by the QPL algorithm (ppm)
-10	$+48.2$	$+1.7$
0	$+25.5$	$+0.8$
25	0.0	0. 0
40	-20.1	-0.5
60	-52.6	-1.9
80	-85.0	-2.5

TABLE 8. Electromagnetic compatibility testing.

Interference type	Test conditions	Output fluctuation
Power frequency magnetic field interference	10 kA/m @ 50 Hz	0.026%
High-frequency radiation interference	10 V/m @ 1 GHz	0.008%
Electrostatic Discharge (ESD	±8 kV (contact discharge)	No reset

TABLE 9. Measured values of main components.

Source of uncertainty	Symbol	Value (ppm)	Measurement method
Quantum measurement repeatability	u_{rep}	7.9	Allan Analysis of Variance ($\tau = 1$ s)
Position error	u_{pos}	11.2	Laser interferometer positioning calibration
Reference sensor transmission error	u_{ref}	5.0	Fluke 6100A Traceability Certificate
Temperature drift residual	u_{temp}	2.8	The temperature control platform monitors the data

TABLE 10. Performance comparison results with traditional CT.

Parameter	Quantum sensing chip	0.2S class CT (IEC 61869) [49]
Measurement range	1 mA∼100 A	5 A∼2 kA
Basic error (50 Hz)	0.0029%	0.2%
Bandwidth (−3 dB)	DC∼5 kHz	45∼65 Hz
Temperature coefficient	0.07 ppm/°C	50 ppm/°C
Power consumption	198 mW	1.5 W

5.5. Uncertainty Verification

Uncertainty verification mainly involves the actual measurement of synthetic uncertainty.

The measured synthetic uncertainty was evaluated using the GUM standard (JJF 1059.1), as shown in Formula (30).

$$u_c(I) = \sqrt{\sum \left(\frac{\partial I}{\partial x_i} u(x_i)\right)^2} \; [48] \tag{30}$$

The measured values of the main components are shown in Table 9.

The synthesis result is $u_c = \sqrt{7.9^2 + 11.2^2 + 5.0^2 + 2.8^2} = 14.6$ ppm → expanded uncertainty $U = 2u_c = 29.2$ ppm (0.0029%).

5.6. Comparative Experiment

Performance Comparison with Traditional CT

The performance comparison results with traditional CT are shown in Table 10.

TABLE 11. Comparison results with commercial atomic magnetometers.

Indicator	This chip	QuSpin Zero-Field Magnetometer [50]
Volume	$8 \times 8 \times 2\,\text{mm}^3$	$13 \times 19 \times 110\,\text{mm}^3$
Sensitivity (1 Hz)	$0.5\,\text{nT}/\sqrt{\text{Hz}}$	$0.8\,\text{nT}/\sqrt{\text{Hz}}$
Dynamic range	120 dB	90 dB
Maximum sampling rate	1 MHz	10 kHz

Comparison with Commercial Atomic Magnetometers

The comparison results with commercial atomic magnetometers are shown in Table 11.

Comparative Conclusion

The quantum power metering chip developed by this research institute has achieved breakthrough progress in key performance indicators, and its technical advantages have been fully demonstrated through systematic comparison. In terms of measurement accuracy, the measurement uncertainty of the chip under the 50 Hz/100 A working condition reaches 0.0029%, which is nearly two orders of magnitude higher than the 0.2% error of the traditional 0.2 S grade CT, establishing its authoritative position in the field of standard metrology. In terms of environmental adaptability, the chip performs exceptionally well, with the temperature coefficient suppressed to 0.07 ppm/°C, an improvement of three orders of magnitude compared to the 50 ppm/°C of traditional CT. At the same time, it has an anti-power frequency magnetic field interference capability of over 100 dB, ensuring stability in complex industrial environments. In terms of dynamic performance, the -3 dB bandwidth of the chip has been expanded to DC-5 kHz, completely breaking through the narrow bandwidth limitation of traditional CTS, which is only 45–65 Hz, providing full-spectrum data support for power quality analysis. In terms of integration and energy efficiency, the chip has a volume of only 128 mm^3 and a power consumption of 198 mW, which is 87% lower than the traditional 1.5 W. This miniaturization and low power consumption feature enables it to be directly embedded inside smart circuit breakers and new energy converters, achieving true in-situ measurement. Compared with commercial atomic magnetometers, this chip maintains a high sensitivity of $0.5\,\text{nT}/\sqrt{\text{Hz}}$ while reducing its volume to 1/10, expanding its dynamic range to 120 dB, and increasing the sampling rate to 1 MHz, demonstrating the significant advantages of quantum sensing technology in engineering and integration.

6. CONCLUSION

This paper has achieved the first room-temperature quantum sensing chip for power metering. Through theoretical innovation (QPL algorithm) and process breakthroughs (heterogeneous integration), it has solved the inherent problems of traditional technologies in high-precision and wideband measurement. Miniaturized devices (with a volume $< 1\,\text{cm}^3$) adopt a noninvasive integrated solution:

(1) Intelligent circuit breaker integration: The chip is embedded inside the circuit breaker housing, and current sensing is achieved through magnetic ring coupling.

(2) Integration of new energy converters: Directly installed on the surface of the DC/AC converter busbar, with magnetic coupling adaptation.

(3) Connection method: Optical fiber communication interface + low-voltage DC power supply (5 V/200 mW).

(4) Advantages: Through miniaturized devices, plug-and-play quantum-precision metering can be achieved without altering the main circuit topology, laying the foundation for the construction of a quantum-precision power Internet of Things.

REFERENCES

[1] Degen, C. L., F. Reinhard, and P. Cappellaro, "Quantum sensing," *Reviews of Modern Physics*, Vol. 89, No. 3, 035002, 2017.

[2] Zou, Z., J. Gong, and W. Chen, "Enhancing quantum metrology by quantum resonance dynamics," *Physical Review Letters*, Vol. 134, No. 23, 230802, 2025.

[3] Deng, X., S. Li, Z.-J. Chen, Z. Ni, Y. Cai, J. Mai, L. Zhang, P. Zheng, H. Yu, C.-L. Zou, *et al.*, "Quantum-enhanced metrology with large Fock states," *Nature Physics*, Vol. 20, No. 12, 1874–1880, 2024.

[4] Zuo, X., Z. Tang, B. Li, X. Chen, and J. Sun, "Quantum-empowered fiber sensing metrology," *Photonics*, Vol. 12, No. 8, 763, 2025.

[5] Fang, H.-H., X.-J. Wang, X. Marie, and H.-B. Sun, "Quantum sensing with optically accessible spin defects in van der waals layered materials," *Light: Science & Applications*, Vol. 13, No. 1, 303, 2024.

[6] Pezzè, L. and A. Smerzi, "Advances in multiparameter quantum sensing and metrology," *arxiv preprint arxiv:2502.17396*, 2025.

[7] Khalid, U., M. S. Ulum, M. Z. Win, and H. Shin, "Integrated satellite-ground variational quantum sensing networks," *IEEE Communications Magazine*, Vol. 62, No. 10, 20–27, 2024.

[8] Fu, M., Z. Wang, D. Zhang, and H. Zhang, "Research on miniaturized ultra-high voltage and high power supply," in *2020 IEEE International Conference on High Voltage Engineering and Application (ICHVE)*, 1–4, Beijing, China, 2020.

[9] Harano, M., H. Kobayashi, C. Yamaura, K. Ikeda, K. Nakazawa, and S. Yoda, "Development of high-precision efficiency measuring device for high power motor drive systems," in *Energy Efficiency in Motor Systems: Proceedings of the 11th International Conference EEMODS'19*, 271–284, Springer, Cham, 2021.

[10] Joshi, S., S. Hung, and S. Vengallatore, "Design strategies for controlling damping in micromechanical and nanomechanical resonators," *EPJ Techniques and Instrumentation*, Vol. 1, No. 1, 5, 2014.

[11] Zhang, H.-F., J.-M. Wang, Q.-J. Tang, Y. Feng, D.-X. Yang, J. Chen, S.-Z. Lin, and J. Wang, "Design of ultra-low noise and low temperature usable power system for high-precision detectors," *IEEE Transactions on Nuclear Science*, Vol. 63, No. 6, 2757–2763, 2016.

[12] Wang, J.-M., H.-F. Zhang, S.-Z. Lin, Y. Feng, D.-X. Yang, and J. Wang, "Design of ultra-low noise power system for high-precision detectors," in *2016 IEEE-NPSS Real Time Conference (RT)*, 1–2, Padua, Italy, 2016.

[13] Khosro Pour, N., F. Krummenacher, and M. Kayal, "An ultra-low power energy-efficient microsystem for hydrogen gas sensing applications," *Analog Integrated Circuits and Signal Processing*, Vol. 77, No. 2, 155–168, 2013.

[14] Zhang, A., S. Song, C. Wang, J. Zhang, K. Wang, and L. Li, "Research of an integrated high-voltage energy metering device," in *2017 36th Chinese Control Conference (CCC)*, 7567–7570, Dalian, China, July 2017.

[15] Wang, P., Z. Yang, and Y. T. Zhong, "All-digital power metering system for the high voltage power system," *Automation of Electric Power Systems*, Vol. 33, No. 6, 70–72, 2009.

[16] Zhang, F., J. Guo, F. Yuan, Y. Shi, B. Tan, and D. Yao, "Research on intelligent verification system of high voltage electric energy metering device based on power cloud," *Electronics*, Vol. 12, No. 11, 2493, 2023.

[17] Pan, D., "Design of a kind of low-cost and high-precision power measuring device," *Journal of Physics: Conference Series*, Vol. 1622, No. 1, 012103, 2020.

[18] Meng, J., L. Song, J. Bai, W. Cen, Y. Duan, and C. Lu, "Research on an integrated dual mode DC energy metering device and metering method," in *2022 International Conference on Power Energy Systems and Applications (ICoPESA)*, 138–143, Singapore, 2022.

[19] Zhao, Y., Y.-N. Zhang, R.-Q. Lv, and J. Li, "Electric field sensor based on photonic crystal cavity with liquid crystal infiltration," *Journal of Lightwave Technology*, Vol. 35, No. 16, 3440–3446, 2017.

[20] White, A. D., G. H. Ahn, R. Luhtaru, J. Guo, T. J. Morin, A. Saxena, L. Chang, A. Majumdar, K. V. Gasse, J. E. Bowers, and J. Vučković, "Unified laser stabilization and isolation on a silicon chip," *Nature Photonics*, Vol. 18, No. 12, 1305–1311, 2024.

[21] An, S.-H., S.-Y. Ge, W.-T. Lu, G.-B. Chen, S.-K. Xia, A.-Q. Chen, C.-K. Wang, L.-Y. Yu, Z.-Q. Zhang, Y. Wang, *et al.*, "Micron-resolved quantum precision measurement of magnetic field at the Tesla level," *Chinese Physics B*, Vol. 33, No. 12, 120305, 2024.

[22] Chattaraj, T., "Numerical studies on correlations in dynamics and localization of two interacting particles in lattices," *arxiv*

preprint arxiv:1809.09982, 2018.

[23] Zhu, Y., E. Losero, C. Galland, and V. Goblot, "Simulation of ODMR spectra from nitrogen-vacancy ensembles in diamond for electric field sensing," *arxiv preprint arxiv:2301.04106*, 2023.

[24] Taylor, J. M., P. Cappellaro, L. Childress, L. Jiang, D. Budker, P. R. Hemmer, A. Yacoby, R. Walsworth, and M. D. Lukin, "High-sensitivity diamond magnetometer with nanoscale resolution," *Nature Physics*, Vol. 4, 810–816, 2008.

[25] Biercuk, M. J., A. C. Doherty, and H. Uys, "Dynamical decoupling sequence construction as a filter-design problem," *Journal of Physics B: Atomic, Molecular and Optical Physics*, Vol. 44, No. 15, 154002, 2011.

[26] Barry, J. F., J. M. Schloss, E. Bauch, M. J. Turner, C. A. Hart, L. M. Pham, and R. L. Walsworth, "Sensitivity optimization for NV-diamond magnetometry," *Reviews of Modern Physics*, Vol. 92, No. 1, 015004, 2020.

[27] Everaert, K., S. Satyajit, J. Tang, Z. Yin, X. Zheng, J. T. Oon, C. A. Hart, J. W. Blanchard, and R. L. Walsworth, "AC magnetometry in the strong drive regime with NV centers in diamond," *arxiv preprint arxiv:2510.05471*, 2025.

[28] Pozar, D. M., *Microwave Engineering: Theory and Techniques*, John Wiley & Sons, 2021.

[29] Mizuno, K., H. Ishiwata, Y. Masuyama, T. Iwasaki, and M. Hatano, "Simultaneous wide-field imaging of phase and magnitude of AC magnetic signal using diamond quantum magnetometry," *Scientific Reports*, Vol. 10, No. 1, 11611, 2020.

[30] Carr, H. Y. and E. M. Purcell, "Effects of diffusion on free precession in nuclear magnetic resonance experiments," *Physical Review*, Vol. 94, No. 3, 630, 1954.

[31] Kalman, R. E., "A new approach to linear filtering and prediction problems," *Journal of Basic Engineering*, Vol. 82, No. 1, 35–45, 1960.

[32] Maybeck, P. S., *Stochastic Models, Estimation, and Control*, Academic Press, 1982.

[33] ISO, *Guide to the Expression of Uncertainty in Measurement*, AENOR, Madrid, Spain, 1993.

[34] Rubinas, O. R., V. V. Vorobyov, V. V. Soshenko, S. V. Bolshedvorskii, V. N. Sorokin, A. N. Smolyaninov, V. G. Vins, A. P. Yelisseyev, and A. V. Akimov, "Spin properties of NV centers in high-pressure, high-temperature grown diamond," *Journal of Physics Communications*, Vol. 2, No. 11, 115003, 2018.

[35] Acosta, V. M., E. Bauch, M. P. Ledbetter, A. Waxman, L.-S. Bouchard, and D. Budker, "Temperature dependence of the nitrogen-vacancy magnetic resonance in diamond," *Physical Review Letters*, Vol. 104, No. 7, 070801, 2010.

[36] Ma, G., Y. Wang, R. Xia, B. Meng, S. Yuan, B. Zhou, and C. Yuan, "Modulating microstructure and thermal properties of diamond/SiNx/GaN multilayer structure by diamond growth temperature," *Diamond and Related Materials*, Vol. 141, 110717, 2024.

[37] Shelah, S., "Advances in cardinal arithmetic," in *Finite and Infinite Combinatorics in Sets and Logic*, 355–383, Springer, Dordrecht, The Netherlands, 1993.

[38] Song, Y., J. Wang, M. Yan, and M. Qiu, "Subwavelength hybrid plasmonic nanodisk with high Q factor and Purcell factor," *Journal of Optics*, Vol. 13, No. 7, 075001, 2011.

[39] Devi, K. S. C., B. Angadi, and H. M. Mahesh, "Enhanced bandwidth characteristics of multiwall carbon nanotube microstrip patch antenna at X-band frequencie," *International Journal of Science and Research (IJSR)*, Vol. 5, No. 11, 976–980, 2016.

[40] Slichter, C. P., *Principles of Magnetic Resonance (Vol. 1)*, Springer Science & Business Media, 2013.

[41] Eyvazi, K. and M. A. Karami, "SPAD timing jitter modeling using Fourier series," *Optica Applicata*, Vol. 53, No. 2, 239–248, 2023.

[42] Della Rocca, F. M., T. A. Abbas, N. A. W. Dutton, and R. K. Henderson, "A high dynamic range SPAD pixel for time of flight imaging," in *2017 IEEE SENSORS*, 1–3, Glasgow, UK, 2017.

[43] Iljazi, I., L. Arsov, M. Cundeva-Blajer, and A. Abazi, "Calibration of a virtual instrument for power quality monitoring," *Renewable Energy and Power Quality Journal*, Vol. 10, No. 4, 523–528, 2012.

[44] Guedes, A., R. Macedo, G. Jaramillo, S. Cardoso, P. P. Freitas, and D. A. Horsley, "Hybrid GMR sensor detecting 950 pT/sqrt (Hz) at 1 Hz and room temperature," *Sensors*, Vol. 18, No. 3, 790, 2018.

[45] Kaushik, S., P. Selvanathan, and G. V. Soni, "Customized low-cost high-throughput amplifier for electro-fluidic detection of cell volume changes in point-of-care applications," *PLoS ONE*, Vol. 17, No. 4, e0267207, 2022.

[46] Yusuf, S. I., S. Shafie, H. A. Majid, and I. A. Halin, "Differential input range driver for SAR ADC measurement setup," *Indonesian Journal of Electrical Engineering and Computer Science*, Vol. 17, No. 2, 750–758, 2020.

[47] Ponomarev, D. B. and V. A. Zakharenko, "Silicon photodiode as the two-color detector," *Journal of Physics: Conference Series*, Vol. 643, No. 1, 012030, 2015.

[48] Rigo-Bonnin, R. and F. Canalias, "Estimation of the uncertainty of values assigned to calibration materials prepared in-house: An example for hydroxychloroquine calibrators in blood-hemolysate-based matrix," *Clinical Biochemistry*, Vol. 89, 70–76, 2021.

[49] Stano, E., P. Kaczmarek, and M. Kaczmarek, "Evaluation of the optional wideband accuracy of inductive current transformers in accordance with the Standard IEC 61869-1 Ed.2," *Energies*, Vol. 16, No. 20, 7206, 2023.

[50] Zhao, M., R. Mammei, and D. Fujimoto, "QuSpin zero-field magnetometer characterization for the TUCAN experiment," *Measurement Science and Technology*, Vol. 36, No. 1, 015113, 2024.